A 17 year climatology of convective cloud top heights in Darwin

Robert C. Jackson[1], Scott M. Collis[1], Valentin Louf[2], Alain Protat[3], and Leon Majewski[3]

[1]Argonne National Laboratory, 9700 Cass Ave., Lemont, IL, USA
[2]School of Earth, Atmosphere and Environment, Monash University, Clayton, VIC, Australia
[3]Bureau of Meteorology, 700 Collins St, Docklands VIC 3208, Australia

Correspondence to: Robert Jackson (rjackson@anl.gov)

Abstract.

The validation of convective processes in general circulation models requires the use of large datasets that provide long term climatologies of the spatial statistics of convection. To that regard, echo top heights (ETHs) retrieved from 17 years of data from C-band POLarization (CPOL) Radar are analyzed in varying phases of the Madden-Julian Oscillation (MJO) and

5 Northern Australian Monsoon in order to provide ample validation statistics for the Department of Energy's next generation Earth Energy Exascale Model. In this paper, ETHs are retrieved using a novel methodology that uses the texture of radial velocity. Comparisons of retrieved ETHs against satellite retrieved cloud top heights from the split window technique show that the estimated ETH are correlated with, and, on average, are within 3 km of satellite retrieved cloud top heights. Using this technique gives comparable ETHs compared to using a reflectivity threshold.

10 Bimodal distributions of ETH, likely attributable to the cumulus congestus and mature stages of convection, are more commonly observed when the active phase of the MJO is away from Australia. The presence of a convectively stable layer at around 5 km altitude over Darwin inhibiting convection past this level can explain the position of the modes at around 5 to 6 km and 12 to 13 km respectively. The spatial distributions show that Hector, a deep convective system that occurs almost daily during the wet season over the Tiwi Islands, and seabreeze convergence lines are likely more common in break conditions.

15 Oceanic mesoscale convective systems (MCSs) are likely more common during the night. Unimodal distributions of ETH are more common during monsoon conditions and during an active MJO over Darwin, consistent with the presence of widespread MCSs that are commonly associated with both the MJO and the Northern Australian Monsoon. In general, the MJO is a greater control of the ETHs observed over Darwin, with generally both lower and more unimodal distributions of ETH when the MJO is active over Darwin.

1 Introduction

Convection in the tropics has an important impact on the global radiative budget. For example, anvil cirrus that are detrained from convection can have a radiative forcing on the order of $100\ W\ m^{-2}$ (Jensen et al., 1994). The infrared radiative forcing

of these anvil cirrus is highly dependent on the temperature, or height where they are present. Furthermore, convection acts as a vehicle to transport moisture to the tropical tropopause layer (15 km) (TTL) (Dessler, 2002) and therefore can significantly affect the distribution of moisture at the tropopause. Therefore, knowledge on the cloud top heights of such convection is needed to determine the impact of deep convection on the global radiative budget and upper tropospheric distribution of moisture and

5 provides the need for a climatology of cloud top heights in the tropics that can be used to validate global climate model (GCM) simulations of convection.

A region in the tropics with continuous observations of cloud top heights provides such a climatology. Such a region is located in Darwin, Australia. Decades of continuous observations have been collected in Darwin, including 17 years of plan position indicator (PPI) scans from the C-band Polarization Radar (CPOL). This region is also ideal for developing such a

10 climatology as the synoptic scale forcing can be objectively determined from both determining information about the Northern Australian Monsoon (Drosdowsky, 1996; Pope et al., 2009a) and about the phase of the MJO (Madden and Julian, 1971; Wheeler and Hendon, 2004), both of which can provide the forcing necessary for convection to develop over the Darwin area. For example, high (20-30 dBZ) reflectivities above the freezing level and greater amounts of lightning have been observed during break convection while monsoonal convection tends to be shallower, more widespread, and less electrically active

15 (Rutledge et al., 1992; Williams et al., 1992; May and Ballinger, 2007; Kumar et al., 2013a, b). Also, the monsoon preferentially onsets when the convectively active phase of the MJO approaches Darwin (Evans et al., 2014), so the MJO and the monsoon are not necessarily independent of each other. Besides convection associated with the MJO and the monsoon, the convection that occurs in this region can also be influenced by the seabreeze and Tiwi Islands, such as the nearly daily summer occurrence of of an intense deep convective system called Hector (Keenan et al., 1989; Crook, 2001). Given the MJO is poorly resolved in

20 many general circulation models (GCMs) (Gu et al., 2011), and that convective parameterizations in GCMs are poor, statistical analyses of how the cloud tops vary for differing phases of the MJO and monsoon are useful for GCM validation of convective processes in models such as the Department of Energy's Energy Earth Exascale Model (E3SM).

Past studies have examined the cloud top heights in convection over Darwin and the maritime continent estimated by radar through the echo top height (ETH). Observations in Indonesia by Johnson et al. (1999) showed 3 modes in ETH in convection

25 during the Tropical Ocean - Global Atmosphere Coupled Ocean Atmospheric Response experiment that corresponded to stable layers: a mode at 2 km, a mode at around 5 km, and a mode at around the tropopause of 15 km. Over Darwin, May and Ballinger (2007) examined the distribution of ETHs in convection for one wet season in and found limited evidence of multimodal distributions of ETH, but had only considered the maximum cloud top height over a cell's lifetime. Furthermore, they found that cloud top heights in break convection were higher than those in monsoonal convection. Kumar et al. (2013b)

30 analyzed two wet seasons of CPOL data and found evidence of bimodal ETH distributions. They also found that convection formed during active monsoon conditions has lower cloud top heights than convection formed during break conditions similar to May and Ballinger (2007). Kumar et al. (2013a) investigated 3 wet seasons of CPOL data in Darwin and found four differing modes that corresponded to trade wind cumulus, cumulus congestus, deep convection and overshooting convection. Therefore, differing conclusions have been reached on the number of modes of convection that are present over Darwin and the maritime

35 continent.

Atmospheric
Chemistry
and Physics
Discussions

Open Access

This study improves upon past studies looking at cloud top heights in Darwin in various ways. First, the analysis is expanded to the full CPOL record of 17 wet seasons to perform the analysis on a more statistically representative dataset than has been done in Johnson et al. (1999); May and Ballinger (2007); Kumar et al. (2013a, b). This is possible using recent advances in supercomputing and recent developments of highly customizable distributed data analysis packages written in Python such as

5 Dask (Dask Development Team, 2016). Secondly, none of the past studies have looked at how ETHs can vary for differing phases of the MJO. Rauniyar and Walsh (2016) have found that rainfall rates in Darwin are correlated to the presence of the convective phase of the MJO over Darwin. Also, Evans et al. (2014) have observed that the preferential onset of the monsoon is when the active phase of the MJO approaches Australia. Therefore it is worth exploring the possibility that cloud top heights of convection in Darwin are also influenced by the MJO. In this study we wish to answer the following questions:

10 1. Does the MJO have an influence on the observed convective cloud top heights over the Darwin area?

2. Do the conclusions of past studies regarding the heights of break and monsoonal convection over Darwin extend to 17 wet seasons?

3. What are the spatial distributions and diurnal cycles of convective cloud top heights over Darwin during the differing phases of the MJO and monsoon?

15 4. When do we observe multiple modes in the distributions of cloud top heights when looking at 17 years worth of data?

It is also important to note that these past studies have used a reflectivity (Z) threshold to determine the ETH, which can underestimate the cloud top height since this criteria would filter out regions of cloud without precipitation that are still detectable by CPOL. Therefore, this study also demonstrates the applicability of a new algorithm that uses velocity texture σ to derive the ETH. Finally, an uncertainty analysis is performed where ETHs are compared against satellite retrieved cloud top heights

20 in order to quantify the uncertainty in the radar estimated cloud top heights and to assess the feasibility of using the velocity texture technique.

The remainder of the paper is organized as follows. Section 2 will go into detail about the data products that are used. Section 3 describes the algorithms used to process the radar data, estimate echo top height, and quantify the synoptic scale forcing over Darwin. Section 4 shows results on how the ETHs vary in differing phases of the MJO, differing monsoonal regimes. Section

25 4 also shows the diurnal cycle of ETHs over Darwin over varying regions and in various phases of the MJO and monsoon in order to link the ETHs to both large scale and localized mechanisms. Section 5 shows the primary conclusions of this study.

2 Data products

2.1 CPOL

The C-band Polarization (CPOL) radar, located at the Tropical Western Pacific (TWP) Atmospheric Radiation Measurement

30 site in Darwin, Australia (Keenan et al., 1998), conducted Plan Position Indicator (PPI) scans every 10 minutes at 15 elevations ranging from 0.5° to 40° during the summer seasons of 1998 to 2017, excluding 2007 and 2008. While CPOL records polarimetric variables, the variables of interest from CPOL for retrieving ETH are the reflectivity Z and the radial velocity v_r. Other instrumentation was used to supplement information provided by CPOL. Rawinsonde launches were conducted four times per

day from the ARM ACRF TWP site, providing vertical profiles of temperature T, dew point T_d, relative humidity RH, and the zonal (u) and meridional (v) components of the wind velocity. In order to estimate the uncertainty in the retrieved ETHs from CPOL, we compare the ETHs against satellite retrieved cloud top heights. To do this, we use the Japanese Multi-functional Transport Satellites (MTSAT) which images brightness temperature T_b every hour at a 1 km resolution, giving information on

5 cloud top heights estimated by the split window technique (Ohkawara, 2004). The MTSAT are integrated into the VISST data product (Minnis et al., 2011) providing cloud top height over a 12° by 12° region centered over Darwin.

3 Data processing algorithms

3.1 Radar data processing

The previous section gave information about the radars and other instruments used in this study. This section details how the

10 echo top heights were estimated from CPOL and evaluated against satellite measurements. The Python ARM Radar Toolkit (Py-ART) (Helmus and Collis, 2016) was used in order to process, grid, and display v_r and Z. The velocity texture was calculated using the standard deviation of the 3 x 3 window surrounding a gate and then was gridded onto a Cartesian grid at a 1 km horizontal and 0.5 km vertical resolution using Barnes (1964)'s interpolation technique. Since at higher elevations and ranges some gaps in the interpolated radar field may be present due to lack of radar sampling at a given location, a radius

15 of influence that increases as a function of distance from the radar was used in order to minimize artifacts generated by radar sampling. Due to the increasing beam width as a function of distance from the radar as well as decreased vertical resolution with height, there is greater uncertainty in the the ETH as distance increases from the radar. Therefore, only data on a 200 by 200 km box surrounding CPOL was used, following (Kumar et al., 2013b) and data less than 20 km from the radar was excluded as the radar does not scan at heights of 20 km at these distances. We use Dask (Dask Development Team, 2016), a

20 package written in Python to analyze datasets on distributed clusters, to map the problem of analyzing the 17 years of CPOL data to the Bebop cluster at Argonne National Laboratory.

3.2 Calculation of ETHs

Now that the radar data has been processed and interpolated onto a Cartesian grid, the next step is to calculate the ETH from CPOL. Past studies (May and Ballinger, 2007; Kumar et al., 2013a, b) have used the highest pixel in the column with Z > 5

25 dBZ as the ETH. Since this threshold can be at least 2 dB above the minimum detectable signal at a range within 100 km of CPOL as seen in Figure 1, using reflectivity (Z) could potentially remove regions that are both detected by CPOL and in cloud, especially for clouds with heights < 10 km and ranges < 60 km from CPOL. Therefore, we examine the possibility in this study of using Doppler velocity texture σ as a threshold instead of Z. To demonstrate that higher values of σ correspond to noise, Figs. 2a,b show an example field of Z and σ from CPOL for a case of isolated convection on 05 March 2006. Figure 2b

30 shows isolated regions of $\sigma < 3$, corresponding to the regions of precipitation that are seen in Figure 2b. The more widespread regions of $\sigma > 3$ correspond to clutter, noise, and multi-trip echoes that are present in Fig. 2a. Furthermore, when a threshold of

$\sigma > 3$ is used to mask gates in Fig. 2a, Fig. 2c shows that only regions of precipitation are still present after masking. Therefore, using σ as a threshold is reasonable for removing regions of noise.

However, even despite using a methodology that automatically determines the minimum detectable signal using σ, there is still the possibility that the cloud water droplets and ice crystals with maximum dimensions below about 0.5 mm are not

5   detected by CPOL. Furthermore, some regions of precipitation were removed in Figure 2c since a few gates with precipitation have higher σ. Therefore, it is important to assess quantitatively whether the ETHs calculated using the σ threshold represent the variability in cloud top heights that is observed in convection in Darwin. To do this, ETHs from CPOL are compared against cloud top heights retrieved by MTSAT which provide an independent estimate of cloud top height. Since the MTSAT data are at an hourly temporal resolution, only CPOL scans that were within 10 minutes of a MTSAT record were compared against the

10   MTSAT retrieved cloud top heights for the months of January and February 2006.

Figure 3 shows the results of such comparisons using both the Z threshold of > 5 dBZ from May and Ballinger (2007) and Kumar et al. (2013a) (Figure 3a) and varying thresholds of σ for the ETHs. In all panels of Figure 3, there is considerable spread in the comparison between the satellite cloud top heights and the ETHs retrieved by CPOL. However, there is a clear peak in the normalized frequency distribution present in all panels at ETHs > 7.5 km and the median ETH is within 3 km of

15   the VISST retrieved cloud top height for ETHs > 2.5 km. Furthermore, the average ETH retrieved from CPOL increases with increasing MTSAT retrieved cloud top height in Figure 3, showing that the ETHs retrieved from CPOL are correlated (Pearson correlation coefficient of 0.49) with the satellite retrieved cloud top heights. As cloud top heights retrieved by MTSAT can have an uncertainty as high as 3 km (Hamada and Nishi, 2010), it is not possible to determine whether the MTSAT retrieved cloud top heights or CPOL ETHs provide the better estimate of cloud top height. Nevertheless, the correlation between the CPOL

20   ETHs and satellite retrieved cloud top heights shows that the CPOL retrieved ETHs using σ threshold captures the variability in cloud top heights that are observed in Darwin.

In Figure 3a, when the May and Ballinger (2007) methodology is used to determine ETH the results are similar to Figure 3c and d, showing that, whether Z or σ are used to retrieve ETH, similar conclusions can be drawn. However, when using a threshold of $\sigma = 2$, the spread is greater in Figure 3b, as shown by the increased difference in the 95th and 5th percentiles in

25   Figure 3b compared to the other thresholds, indicating a reduced correlation between ETH and MTSAT-retrieved cloud top height compared to using the other thresholds to calculate ETH. The mean, and 5th and 95 percentiles are similar in Figure 3acd, showing that there is little difference between using May and Ballinger (2007) and Kumar et al. (2013a)'s technique compared to using σ for calculating ETH. Therefore, this study uses the highest gate where $\sigma < 3$ as the ETH, as there is little difference in the estimates of cloud top heights between using Z and using σ.

30   ## 3.3   Quantification of large scale forcing

Now that a methodology has been developed to estimate the cloud top height from the CPOL data, the next step in this study is to develop methodologies for quantifying the large scale forcing in the Darwin region. The large scale forcing in the Darwin region can be quantified with respect to two major synoptic phenomena. One of them is the Northern Australian Monsoon (Drosdowsky, 1996; Pope et al., 2009a). Its presence is characterized by deep westerly winds over Darwin that provide moisture

flow from the Indian Ocean to the Darwin region. Many algorithms have been used in the literature to determine the presence of the Northern Australian Monsoon. However, only Drosdowsky (1996) and Pope et al. (2009a) robustly identify the presence of the monsoon. These algorithms depend on the profile of the zonal component u and meridional component v of the wind as well as temperature, dew point, and pressure collected by rawinsondes over Darwin. The first, Drosdowsky (1996), uses the

5   deep-layer (Surface-500 hPa) mean u in order to characterize the presence of the monsoon. Under this classification, a deep layer of westerly winds is characteristic of the monsoon, which provides an environment where moisture is flowing from the Indian Ocean to Darwin. The second, Pope et al. (2009a), uses k-means clustering on the winds, temperature, and dew point to find five regimes that correspond to differing synoptic scale phenomena in Darwin: deep west, moist east, east, dry east, and shallow west. The "deep west" and "shallow west" regimes corresponds to westerly flow from the surface to 500 hPa, or the

10   active monsoon. The "moist east" regime corresponds to (Drosdowsky, 1996)'s "break" regime where continental convection is more likely to occur, and the other regimes correspond to either suppressed or transitional regimes.

     The large scale forcing can also be quantified by the phase of the Madden-Julian Oscillation (Madden and Julian, 1971). The phase of the MJO is quantified using a number 1 to 8 that gives an indicator of the position of the enhanced and suppressed convective activity associated with the MJO. When the MJO phase increases from 1 to 3, the enhanced convective activity

15   is traveling to the east from the Indian Ocean. When the MJO index increases from 4 to 7, the enhanced convective activity is over the maritime continent and traveling east to the Pacific Ocean. When the MJO index is 8, the enhanced convective activity is over the Pacific Ocean. This MJO index is determined using Wheeler and Hendon (2004)'s database that is based on both the outgoing long-wave radiation and the 850 to 200 hPa u from reanalysis data. Rauniyar and Walsh (2016) found that the yearly occurrence of the Pope et al. (2009a) regimes has a high amount of interannual variability as they are modulated

20   by the El Nino-Southern Oscillation (ENSO) while the occurrence of the MJO does not. Therefore, the use of Pope et al. (2009a) is less suitable for a sample size of 17 seasons than the use of the MJO for analyzing such a dataset. Furthermore, the five classifications provide more opportunity for over-classification than using Drosdowsky (1996). Therefore, to quantify the large scale forcing over Darwin, the dataset is separated using only the MJO index and the Drosdowsky (1996) monsoon classification. To even further prevent the possibility of over-classification, much of the data in this study are classified into

25   whether the convective phase of the MJO is over Australia (MJO indicies 4 to 7), or when it is not (MJO indicies 1 to 3, 8).

     Figures 4 and 5 show the mean thermodynamic and wind profiles for given phases of the MJO and monsoon. Fig. 4 shows that break conditions are generally characterized by a layer of east-northeasterly winds extending to about 10 km when the MJO is over Australia and throughout the troposphere when the convective mode of the MJO is elsewhere, while westerlies are prevalent at altitudes up to 8 km during monsoon conditions. This, and the profiles of temperature and dew point point to

30   greater advection of moisture from the Indian Ocean to Darwin during monsoonal conditions and drier air from Australia in break conditions.

     The thermodynamic profiles in Figures 4 and 5 show a transition from convectively unstable conditions from the surface until 4 km to stable at around 4-6 km, or temperatures around $0°C$ with the tropopause located at around 15 km. Three stable layers over Indonesia were observed by Johnson et al. (1999): a trade wind layer at 2 km, a stable layer at around 6 km, and

35   the tropopause at 15 km. This suggests that, while the trade wind stable layer is not present over Darwin, the stable layer at

around around $0°C$ that is present over Indonesia is also present over Darwin. The presence of such a layer suggests that any parcel lifted from the surface would easily rise to heights to around 4-6 km, or $0°C$ but would need to be dynamically energetic enough to penetrate through the stable layer above this level. Furthermore, since the stable layer is located at temperatures just below $0°C$, this inhibits the formation of ice which releases latent heat that would invigorate the updraft, further inhibiting

5   convection. Therefore, an updraft strong enough to reach levels where ice formation to occur would be more likely able to penetrate up to the tropopause. This notion is supported by the observations of vertical velocities in convection that reaches the tropopause typically being strongest above 5 km (May and Rajopadhyaya, 1999; Collis et al., 2013; Varble et al., 2014). This therefore indicates that the thermodynamic profiles favor the formation of two distinct populations of convection: weaker cumulus congestus that do not penetrate heights much past the stable layer and stronger deep convection that would more than

10 likely be able to penetrate the tropopause.

4   Statistical analysis/discussion

4.1   p.d.f.s of ETH

The previous section detailed the methods and uncertainties in the derived ETHs and gave a meteorological overview of the differing synoptic scale regimes. In this section, the entire 17 year record of ETHs in differing synoptic scale regimes

15 is analyzed in order to provide a climatology of convective cloud top heights. In this analysis, only convective regions are considered, using the Steiner et al. (1995) to define convective regions which uses both a threshold of $Z > 40$ dBZ as well as the peakedness of the Z field in order to classify regions as convective. This algorithm was designed for convection in the Tropics, and a visual analysis of the algorithm showed that it reasonably distinguished between stratiform and convective regions (not shown).

20   Figure 6 shows the p.d.f.s of ETHs in differing MJO indicies and monsoonal classifications. Some of the distributions shown in Figure 6 are bimodal with one mode at an ETH of approximately 4 to 8 km and the other at about 9 to 13 km. Two of the modes are therefore similar to the largest two modes observed by Johnson et al. (1999): a mode at approximately 6 km corresponding to the cumulus congestus stage and a mode at 15 km corresponding to deep convection. Kumar et al. (2013a) observed 4 modes, with the trade wind cumulus mode at 2 km, congestus mode at heights of 3-6.5 km, deep convection mode

25 at 6.5 to 15 km, and overshooting convection at heights greater than 15 km. However, since the 2 km modes in Johnson et al. (1999); Kumar et al. (2013a) were observed using measurements with a cloud radar that would be more sensitive to liquid cloud droplets than CPOL, and that there is no inversion at 2 km in Figs. 4, 5, it is not surprising that their trade wind cumulus mode is not observed here. May and Ballinger (2007) observed limited evidence of such bimodality, but bimodal distributions of ETH were also found by Kumar et al. (2013b), corresponding to similar heights. The thermodynamic profiles shown in the

30 previous section can explain the bimodality seen in Figure 6. In particular, the presence of a stable layer at heights above 5 km can explain the bimodality seen in some of the regimes in Figure 6. As convection develops and evolves into deeper convection, it will first have to grow to the height of the start of the stable layer and will stop growing in vertical extent there if there is

not enough buoyancy to penetrate past it. Updrafts would have to be energetic enough to penetrate the cap, and such updrafts would more than likely penetrate up to the tropopause.

In order to quantify the locations and contributions of the peaks in each p.d.f in Figure 6, bimodal Gaussian fits of the form in Equation (1)

$$P(x) = A \frac{1}{\sigma_1 \sqrt{2\pi}} e^{-(x-\mu_1)^2/2\sigma_1^2} + (1-A) \frac{1}{\sigma_2 \sqrt{2\pi}} e^{-(x-\mu_2)^2/2\sigma_2^2} \tag{1}$$

where A is the contribution of mode 1, μ_1, μ_2 are the mean and σ_1 and σ_2 are the standard deviations of modes 1 and 2 respectively were generated for each regime and plotted onto Figure 7. Mode 1 is the mode with smaller ETHs and mode 2 is the mode with larger ETHs. In 7, μ_1 ranges between 4 and 8 km and μ_2 ranges between 9 and 15 km. This shows that the location mode 1 roughly corresponds to the location of the cumulus congestus mode observed by Johnson et al. (1999); Kumar et al. (2013b), and the location of mode 2 corresponding to their deep convective mode. Therefore, for the rest of this paper, mode 1 will be referred to as the cumulus congestus mode and mode 2 the deep convective mode.

The locations of the two modes in Figures 6 and 7 vary with MJO index. As the active phase of the MJO is over Australia (MJO indicies 4 to 7), values of A range from 0.8 to 0.5 while they are 0.3 to 0.5 in break conditions when the active phase of the MJO is away from Australia. The relative unimodality around ETH of 10 to 12 km present when the active phase of the MJO is over Australia suggests that the MJO contributes to an enhanced presence of deep convection, with less such convection when the active phase of the MJO is away from Australia. In monsoon conditions, values of A are greater than 0.65, and greater than 0.9 when the active phase of the MJO is over Australia. This indicates that most of the convection observed during both an active monsoon and active MJO are categorized as deep convection. The presence of mostly deep convection during an active MJO and monsoon is also consistent with an increased presence of widespread mesoscale convective systems (MCSs). Indeed, Virts and Houze (2015) have observed an increased number of MCSes in the tropics during the active phase of the MJO, and Pope et al. (2009b) have observed an increased number of MCSes over northern Australia during active monsoon conditions, which provides further evidence to support this claim.

The locations of these modes also vary depending on whether or not the active phase of the MJO is present over Australia. In Figure 7, on average the cumulus congestus mode is located at 5.4 (6.6 km) when the MJO is active (inactive) over Australia during break conditions. During monsoon conditions, this mode is on average at 5.5 km (7.6 km) when the MJO is active (inactive) over Australia. The average locations of the deep convective mode during break conditions become 11.6 and 12.5 km during active and inactive MJO conditions respectively. For the monsoon, the average locations are 9.5 km and 12.5 km during active and inactive MJO conditions respectively. Therefore, on average, convection is penetrating to higher heights both during break conditions and when the MJO is inactive over Australia. However, the change in heights associated with an active MJO over Australia is greater than that associated with the monsoon. The higher cloud top heights observed during break conditions are consistent the studies of May and Ballinger (2007) and Kumar et al. (2013a) who also noted higher cloud top heights in break convection compared to monsoonal convection, but did not examine how convective cloud top heights varied as a function of MJO index. Evans et al. (2014) noted that the monsoon over Darwin will preferentially onset at MJO indicies

3 and 4, so this suggests that the observations of lower convective cloud top heights during an active monsoon as observed May and Ballinger (2007) and Kumar et al. (2013a) could also be attributable to the active phase of the MJO. Therefore future studies that examine the properties of convection in Darwin in differing large scale conditions must also consider the phase of the MJO in addition to the monsoon, as the MJO has been shown here to be of importance.

4.2   Diurnal cycle and spatial distribution of ETHs

The previous section established that the MJO is a significant control of the ETHs observed over Darwin. However, the mechanisms by which convection over Darwin can be generated can not only depend on the large scale forcing but can also be influenced by localized mechanisms such as seabreezes. Therefore, to investigate under what conditions the formation of convection via localized mechanisms is more likely, Figures 8 and 9 show normalized frequencies of occurrence of ETHs > 7 and < 7 km for the given synoptic scale forcing shown in Figures 4 and 5 as a function of space and time. The threshold of 7 km is shown as it is, on average, the local minimum between the cumulus congestus and deep convective modes in Figure 6. Figure 8 shows that, in break conditions, the cumulus congestus are confined to Tiwi islands and the Australian continent during the day and more confined to the ocean at night. When the MJO is active over Australia, greater counts are present over the ocean during the day than when the active phase is away from Australia. Similar conclusions can be made for deep convection during break conditions in Figure 8.

The peak in deep convection isolated over the Tiwi islands present during the day in Figure 8 is a deep convective system that forms almost daily during the wet season called Hector the Convector (Keenan et al., 1989; Crook, 2001). It is likely forced by seabreeze convergence lines and further intensified by cold pools that formed from neighboring cumulus congestus (Dauhut et al., 2016). Given this, in break conditions, both surface level easterly flow onto the Tiwi Islands providing a seabreeze and the presence of cumulus congestus over the Tiwi Islands in Figure 8 show that the environment is favorable for Hector to occur. The reduced widespread cloud cover that is observed during break conditions (May et al., 2012) also provides an environment more favorable for localized seabreezes to develop around the Tiwi Islands, and hence for Hector to form. A maximum in rainfall over the Tiwi Islands, attributed to Hector, when the MJO is inactive over Australia has been noted by Rauniyar and Walsh (2016). While Figure 10 shows a greater frequency of deep convective ETHs over the Tiwi Islands when the MJO is inactive over Australia during the day, this study extends this conclusion to suggest that Hector is also more active during the day and when the MJO is inactive over Australia. During the night, both congestus and deep convection are more focused towards the oceans and the northern Australian coast in Figure 10. Given that an overnight peak in rainfall in the tropics has been attributed to the presence of long lived oceanic MCSs by Nesbitt and Zipser (2003), and that it is very common for MCSs over Darwin to last over 4 hours (Pope et al., 2009b), this is likely the result of such long lived MCSs. Kumar et al. (2013a) showed a peak in ETHs over the ocean in the early morning hours and over the coast and continents during the afternoon, so this study extends their conclusion to 17 wet seasons of data.

In active monsoon conditions, cumulus congestus are widespread throughout the western half of the region while the deeper convection is mostly focused on the Australian coast in Figure 9. Fewer occurrences of deep convection on the Tiwi islands are present compared to break conditions, suggesting that conditions are less favorable for the formation of Hector during

an active monsoon. Since westerly winds at the surface to 500 hPa are prevalent during an active monsoon, the seabreeze is mostly likely to occur over the western coast of the Tiwi islands and the western Australian coast over Darwin and therefore any seabreeze convergence lines that do form would form there. However, as active monsoon conditions are typically characterized by widespread stratiform cloud cover (May et al., 2012), it is less likely that diurnal solar heating would be as important

5 during an active monsoon. The reduced solar heating during an active monsoon is likely resulting in the reduced occurrences of Hector, as the lack of solar heating decreases the likelihood that localized seabreezes form.

At night, both congestus and deep convection decrease in occurrence on the continents as one goes east. This suggests that oceanic MCSs, common during an active monsoon (May et al., 2012), are decaying as they approach land from the west as would be expected with the deep westerly flow. During the night they would encounter a drier airmass than over the ocean,

10 causing a depletion of moisture and hence decay. Figure 11 also shows more sporadic occurrences of both congestus and deep convection when the MJO is inactive over Australia compared to when it is active. There are 63 days where the MJO was both inactive over Australia and where an active monsoon occurs, while there are 54 days where the monsoon and MJO are both active over Australia. Meanwhile, 7.9×10^5 occurrences of ETH > 7 km are present when the MJO is inactive and 2.5×10^6 are when the MJO is active in Figure 9. Therefore, the more sporadic occurrences are not due to the fact that the monsoon and

15 MJO were active for fewer days, but rather this suggests that, even in the presence of deep westerlies that are characteristic of the monsoon, convection is suppressed when the MJO is inactive over Australia. Indeed, Evans et al. (2014) have found that the onset of the monsoon preferentially starts when the MJO indicies are 3 and 4 and decays when MJO indicies are 7 and 8 as the convective phase travels east over the maritime continent. Therefore, it is not surprising to see fewer occurrences of convection when the MJO is inactive over Australia.

20 To demonstrate how the locations of the modes and total occurrences vary with time of day, Figure 10 shows how the two modes of convection vary as a function of time of day with fits generated from Equation (1) at 2 hour intervals. Figure 10 shows that total counts start to increase at around 400 UTC as convection initiates during the late morning hours and transitions from congestus to deep convection. At sunset, a decrease in the total number of counts is seen, suggesting that the loss of solar heating, an important factor during break conditions (May et al., 2012), is contributing to the decay of convection.

25 The total counts and then show a second peak during the overnight hours with generally bimodal distributions. This secondary peak during the overnight hours, given the oceanic nature of the overnight convection as suggested by Figures 8, 9, are likely due to nocturnal MCSs that are common over the tropical oceanic regions (Nesbitt and Zipser, 2003). In Figure 8, the ETH distributions are generally bimodal throughout the day when the active phase of the MJO is away from Australia, and the overnight peak is less pronounced in these conditions. Since MCSs are larger in extent in the convectively active phase of the

30 MJO (Virts and Houze, 2015), the reduced coverage of MCSs in the inactive phase of the MJO likely explains the decreased contribution of deep convection and hence the bimodality seen. Rather, as suggested by the spatial analysis and Rauniyar and Walsh (2016), Hector and seabreeze convergence lines are more likely contributing to the distributions seen here. During monsoon conditions, Figure 11 shows that a majority of the counts occur when the convective phase of the MJO is over Australia and during the daytime hours. Similar conclusions about the peaks of convective activity and bimodality seen in

35 Figure 10 can be made in Figure 11.

5 Conclusions

Radar estimated echo top heights from convection that was present during 17 wet seasons was scanned by the C-band Polariza-
tion Radar (CPOL) were generated using a velocity-texture based methodology. This methodology differed from past studies
that used reflectivity based thresholds such as May and Ballinger (2007); Kumar et al. (2013a, b). The use of velocity texture
5   provides the potential for an automatic detection of the noise floor which increases the capability of including the lowest re-
flectivties that still correspond to meteorological echoes. It is demonstrated that such a methodology is reasonable to use for
estimating the echo top height as they are correlated with cloud top heights retrieved by brightness temperatures from satellites
(Ohkawara, 2004; Minnis et al., 2011). This comparison also demonstrates the null result when comparing the ETHs against
those retrieved by a reflectivity threshold: the ETHs generated using thresholds based off of velocity texture and reflectivity are
10   similar for convection sampled by CPOL.

These echo top heights are then sorted by the Wheeler and Hendon (2004) MJO index and Drosdowsky (1996) mon-
soon/break classification. Some key conclusions can be made from this data:

1. Bimodal echo top heights were observed, and more common during break conditions, with a peak at around 5 to 6 km and
another around 10 to 12 km, likely corresponding to cumulus congestus and deep convection. The break between these peaks
15   corresponds with the presence of a stable layer at 5 km inhibiting the development of more intermediate convection.

2. Unimodal distributions were more common during an active MJO and an active monsoon, with mostly deep convection
being observed during these periods. This is consistent with past studies suggesting that long lived MCSes are present during
these conditions. In general the MJO is a more important control of cloud top heights than the phase of the monsoon for the 17
years of data shown here, with lower echo top heights observed when the MJO is active over Australia.

20   3. The observed cloud top heights during the day in break and MJO-inactive conditions showed the presence of Hector and
cumulus congestus. Meanwhile, at night, the distributions of echo top heights showing mostly deep convection combined with
the general characteristics of convection observed during the MJO and active monsoon are more consistent with the presence
of widespread long lived MCSes during the night time hours.

4. The fewest occurrences of convection were observed during both an inactive MJO and an inactive monsoon. Given that
25   there were more days observed during an inactive MJO and inactive monsoon than when the MJO and monsoon were active
over Australia, this shows that convection is suppressed during these conditions.

The observed distributions of echo top heights seen here create a suitable climatology for the validation of convective
parameterizations in global climate models and are in the process of being used for the validation of the DOE's E3SM model.
Future studies should focus on the improvement of the representation of the MJO and the monsoon in global climate models,
30   as these results demonstrate the clear importance of both phenomena in determining the properties of convection observed in
Northern Australia. It is also clear from the research presented here that the MJO is important for determining the properties
of convection over Darwin and future studies looking at aspects of convection such as vertical velocities and convective area
should consider the influence of the MJO as well as the monsoon.

Code availability. The code used to generate these plots is available at https://github.com/EVS-ATMOS/cmdv-rrm-anl/. The code used to generate velocity texture is included in the Python Atmospheric Radiation Measurement (ARM) Radar toolkit, available at http://github.com/ARM-DOE/pyart

Data availability. The data used to generate the cloud top height dataset is in the process of being submitted to the Atmospheric Radiation
5 Measurement (ARM) Archive and will be available as a PI product upon publication of this manuscript.

Competing interests. There are no competing interests for this manuscript.

Atmospheric
Chemistry
and Physics
Discussions

References

Barnes, S. L.: A Technique for Maximizing Details in Numerical Weather Map Analysis, Journal of Applied Meteorology, 3, 396–409, https://doi.org/10.1175/1520-0450(1964)003<0396:ATFMDI>2.0.CO;2, https://doi.org/10.1175/1520-0450(1964)003<0396:ATFMDI>2.0.CO;2, 1964.

5 Collis, S., Protat, A., May, P. T., and Williams, C.: Statistics of Storm Updraft Velocities from TWP-ICE Including Verification with Profiling Measurements, Journal of Applied Meteorology and Climatology, 52, 1909–1922, https://doi.org/10.1175/JAMC-D-12-0230.1, https://doi.org/10.1175/JAMC-D-12-0230.1, 2013.

Crook, N. A.: Understanding Hector: The Dynamics of Island Thunderstorms, Monthly Weather Review, 129, 1550–1563, https://doi.org/10.1175/1520-0493(2001)129<1550:UHTDOI>2.0.CO;2, https://doi.org/10.1175/1520-0493(2001)129<1550:UHTDOI>2.0.CO;2, 2001.

10 Dask Development Team: Dask: Library for dynamic task scheduling, http://dask.pydata.org, 2016.

Dauhut, T., Chaboureau, J.-P., Escobar, J., and Mascart, P.: Giga-LES of Hector the Convector and Its Two Tallest Updrafts up to the Stratosphere, Journal of the Atmospheric Sciences, 73, 5041–5060, https://doi.org/10.1175/JAS-D-16-0083.1, https://doi.org/10.1175/JAS-D-16-0083.1, 2016.

15 Dessler, A. E.: The effect of deep, tropical convection on the tropical tropopause layer, Journal of Geophysical Research: Atmospheres, 107, ACH 6–1–ACH 6–5, https://doi.org/10.1029/2001JD000511, http://dx.doi.org/10.1029/2001JD000511, 2002.

Drosdowsky, W.: Variability of the Australian Summer Monsoon at Darwin: 1957–1992, Journal of Climate, 9, 85–96, https://doi.org/10.1175/1520-0442(1996)009<0085:VOTASM>2.0.CO;2, https://doi.org/10.1175/1520-0442(1996)009<0085:VOTASM>2.0.CO;2, 1996.

20 Evans, S., Marchand, R., and Ackerman, T.: Variability of the Australian Monsoon and Precipitation Trends at Darwin, Journal of Climate, 27, 8487–8500, https://doi.org/10.1175/JCLI-D-13-00422.1, https://doi.org/10.1175/JCLI-D-13-00422.1, 2014.

Gu, J.-Y., Ryzhkov, A., Zhang, P., Neilley, P., Knight, M., Wolf, B., and Lee, D.-I.: Polarimetric Attenuation Correction in Heavy Rain at C Band, Journal of Applied Meteorology and Climatology, 50, 39–58, https://doi.org/10.1175/2010JAMC2258.1, https://doi.org/10.1175/2010JAMC2258.1, 2011.

25 Hamada, A. and Nishi, N.: Development of a Cloud-Top Height Estimation Method by Geostationary Satellite Split-Window Measurements Trained with CloudSat Data, Journal of Applied Meteorology and Climatology, 49, 2035–2049, https://doi.org/10.1175/2010JAMC2287.1, https://doi.org/10.1175/2010JAMC2287.1, 2010.

Helmus, J. and Collis, S.: The Python ARM Radar Toolkit (Py-ART), a Library for Working with Weather Radar Data in the Python Programming Language, Journal of Open Research Software, 4, https://doi.org/10.5334/jors.119, http://openresearchsoftware.metajnl.com/articles/10.5334/jors.119/, 2016.

30

Jensen, E. J., Kinne, S., and Toon, O. B.: Tropical cirrus cloud radiative forcing: Sensitivity studies, Geophysical Research Letters, 21, 2023–2026, https://doi.org/10.1029/94GL01358, http://dx.doi.org/10.1029/94GL01358, 1994.

Johnson, R. H., Rickenbach, T. M., Rutledge, S. A., Ciesielski, P. E., and Schubert, W. H.: Trimodal Characteristics of Tropical Convection, Journal of Climate, 12, 2397–2418, https://doi.org/10.1175/1520-0442(1999)012<2397:TCOTC>2.0.CO;2, https://doi.org/10.1175/1520-0442(1999)012<2397:TCOTC>2.0.CO;2, 1999.

35

Keenan, T., Glasson, K., Cummings, F., Bird, T. S., Keeler, J., and Lutz, J.: The BMRC/NCAR C-Band Polarimetric (C-POL) Radar System, Journal of Atmospheric and Oceanic Technology, 15, 871–886, https://doi.org/10.1175/1520-0426(1998)015<0871:TBNCBP>2.0.CO;2, https://doi.org/10.1175/1520-0426(1998)015<0871:TBNCBP>2.0.CO;2, 1998.

Keenan, T. D., Manton, M. J., Holland, G. J., and Morton, B. R.: The Island Thunderstorm Experiment (ITEX)—A Study of Tropical
5   Thunderstorms in the Maritime Continent, Bulletin of the American Meteorological Society, 70, 152–159, https://doi.org/10.1175/1520-0477(1989)070<0152:TITESO>2.0.CO;2, https://doi.org/10.1175/1520-0477(1989)070<0152:TITESO>2.0.CO;2, 1989.

Kumar, V. V., Jakob, C., Protat, A., May, P. T., and Davies, L.: The four cumulus cloud modes and their progression during rainfall events: A C-band polarimetric radar perspective, Journal of Geophysical Research: Atmospheres, 118, 8375–8389, https://doi.org/10.1002/jgrd.50640, http://dx.doi.org/10.1002/jgrd.50640, 2013a.

Kumar, V. V., Protat, A., May, P. T., Jakob, C., Penide, G., Kumar, S., and Davies, L.: On the Effects of Large-Scale Environ-
10   ment and Surface Types on Convective Cloud Characteristics over Darwin, Australia, Monthly Weather Review, 141, 1358–1374, https://doi.org/10.1175/MWR-D-12-00160.1, https://doi.org/10.1175/MWR-D-12-00160.1, 2013b.

Madden, R. A. and Julian, P. R.: Detection of a 40–50 Day Oscillation in the Zonal Wind in the Tropical Pacific, Journal of the Atmospheric Sciences, 28, 702–708, https://doi.org/10.1175/1520-0469(1971)028<0702:DOADOI>2.0.CO;2, https://doi.org/10.1175/
15   1520-0469(1971)028<0702:DOADOI>2.0.CO;2, 1971.

May, P. T. and Ballinger, A.: The Statistical Characteristics of Convective Cells in a Monsoon Regime (Darwin, Northern Australia), Monthly Weather Review, 135, 82–92, https://doi.org/10.1175/MWR3273.1, https://doi.org/10.1175/MWR3273.1, 2007.

May, P. T. and Rajopadhyaya, D. K.: Vertical Velocity Characteristics of Deep Convection over Darwin, Australia, Monthly Weather Review, 127, 1056–1071, https://doi.org/10.1175/1520-0493(1999)127<1056:VVCODC>2.0.CO;2, https://doi.org/10.1175/
20   1520-0493(1999)127<1056:VVCODC>2.0.CO;2, 1999.

May, P. T., Long, C. N., and Protat, A.: The Diurnal Cycle of the Boundary Layer, Convection, Clouds, and Surface Radiation in a Coastal Monsoon Environment (Darwin, Australia), Journal of Climate, 25, 5309–5326, https://doi.org/10.1175/JCLI-D-11-00538.1, https://doi.org/10.1175/JCLI-D-11-00538.1, 2012.

Minnis, P., Sun-Mack, S., Young, D. F., Heck, P. W., Garber, D. P., Chen, Y., Spangenberg, D. A., Arduini, R. F., Trepte, Q. Z., Smith, W. L.,
25   Ayers, J. K., Gibson, S. C., Miller, W. F., Hong, G., Chakrapani, V., Takano, Y., Liou, K. N., Xie, Y., and Yang, P.: CERES Edition-2 Cloud Property Retrievals Using TRMM VIRS and Terra and Aqua MODIS Data 2014; Part I: Algorithms, IEEE Transactions on Geoscience and Remote Sensing, 49, 4374–4400, https://doi.org/10.1109/TGRS.2011.2144601, 2011.

Nesbitt, S. W. and Zipser, E. J.: The Diurnal Cycle of Rainfall and Convective Intensity according to Three Years of TRMM Measurements, Journal of Climate, 16, 1456–1475, https://doi.org/10.1175/1520-0442(2003)016<1456:TDCORA>2.0.CO;2, https://journals.ametsoc.
30   org/doi/abs/10.1175/1520-0442%282003%29016%3C1456%3ATDCORA%3E2.0.CO%3B2, 2003.

Ohkawara, N.: Multi-Functional Transport Satellite (mtsat), https://doi.org/10.1.1.4.8950, http://citeseerx.ist.psu.edu/viewdoc/download?doi=10.1.1.4.8950&rep=rep1&type=pdf, 2004.

Pope, M., Jakob, C., and Reeder, M. J.: Regimes of the North Australian Wet Season, Journal of Climate, 22, 6699–6715, https://doi.org/10.1175/2009JCLI3057.1, https://doi.org/10.1175/2009JCLI3057.1, 2009a.

35 Pope, M., Jakob, C., and Reeder, M. J.: Objective Classification of Tropical Mesoscale Convective Systems, Journal of Climate, 22, 5797–5808, https://doi.org/10.1175/2009JCLI2777.1, https://doi.org/10.1175/2009JCLI2777.1, 2009b.

Rauniyar, S. and Walsh, K.: Spatial and temporal variations in rainfall over Darwin and its vicinity during different large-scale environments, Climate Dynamics, 46, https://doi.org/10.1007/s00382-015-2606-1, https://doi.org/10.1007/s00382-015-2606-1, 2016.

Rutledge, S. A., Williams, E. R., and Keenan, T. D.: The Down Under Doppler and Electricity Experiment (DUNDEE): Overview and Preliminary Results, Bulletin of the American Meteorological Society, 73, 3–16, https://doi.org/10.1175/1520-0477(1992)073<0003:TDUDAE>2.0.CO;2, https://doi.org/10.1175/1520-0477(1992)073<0003:TDUDAE>2.0.CO;2, 1992.

Steiner, M., Jr., R. A. H., and Yuter, S. E.: Climatological Characterization of Three-Dimensional Storm Structure from Operational Radar and Rain Gauge Data, Journal of Applied Meteorology, 34, 1978–2007, https://doi.org/10.1175/1520-0450(1995)034<1978:CCOTDS>2.0.CO;2, https://doi.org/10.1175/1520-0450(1995)034<1978:CCOTDS>2.0.CO;2, 1995.

Varble, A., Zipser, E. J., Fridlind, A. M., Zhu, P., Ackerman, A. S., Chaboureau, J.-P., Fan, J., Hill, A., Shipway, B., and Williams, C.: Evaluation of cloud-resolving and limited area model intercomparison simulations using TWP-ICE observations: 2. Precipitation microphysics, Journal of Geophysical Research: Atmospheres, 119, 13,919–13,945, https://doi.org/10.1002/2013JD021372, http://dx.doi.org/10.1002/2013JD021372, 2013JD021372, 2014.

Virts, K. S. and Houze, R. A.: Variation of Lightning and Convective Rain Fraction in Mesoscale Convective Systems of the MJO, Journal of the Atmospheric Sciences, 72, 1932–1944, https://doi.org/10.1175/JAS-D-14-0201.1, https://doi.org/10.1175/JAS-D-14-0201.1, 2015.

Wheeler, M. C. and Hendon, H. H.: An All-Season Real-Time Multivariate MJO Index: Development of an Index for Monitoring and Prediction, Monthly Weather Review, 132, 1917–1932, https://doi.org/10.1175/1520-0493(2004)132<1917:AARMMI>2.0.CO;2, https://doi.org/10.1175/1520-0493(2004)132<1917:AARMMI>2.0.CO;2, 2004.

Williams, E. R., Geotis, S. G., Renno, N., Rutledge, S. A., Rasmussen, E., and Rickenbach, T.: A Radar and Electrical Study of Tropical "Hot Towers", Journal of the Atmospheric Sciences, 49, 1386–1395, https://doi.org/10.1175/1520-0469(1992)049<1386:ARAESO>2.0.CO;2, https://doi.org/10.1175/1520-0469(1992)049<1386:ARAESO>2.0.CO;2, 1992.

Atmospheric
Chemistry
and Physics
Discussions

Open Access
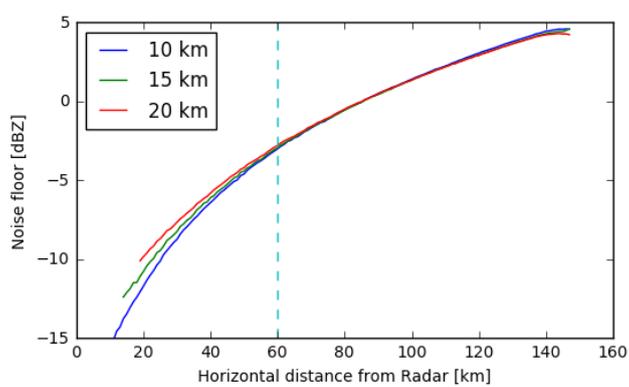
Figure 1. Minimum detectable signal of CPOL as a function of horizontal distance from CPOL for 3 vertical levels.

Atmospheric
Chemistry
and Physics
Discussions

Open Access
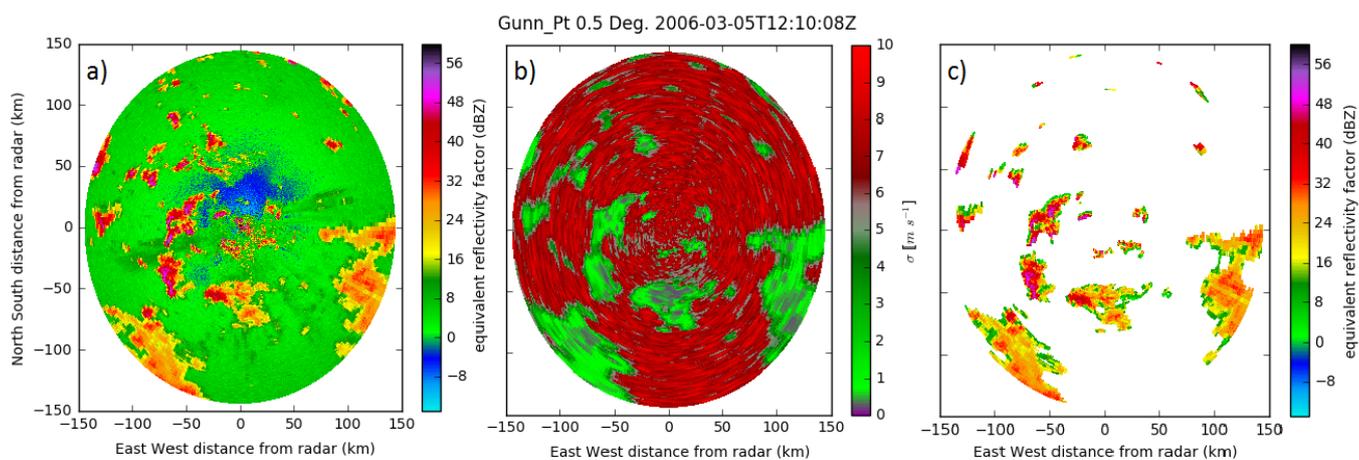
Figure 2. (a) Example Z (a) and (b) σ field for a PPI scan from CPOL on 05 March 2006. (c) Z after masking gates with $\sigma > 3$
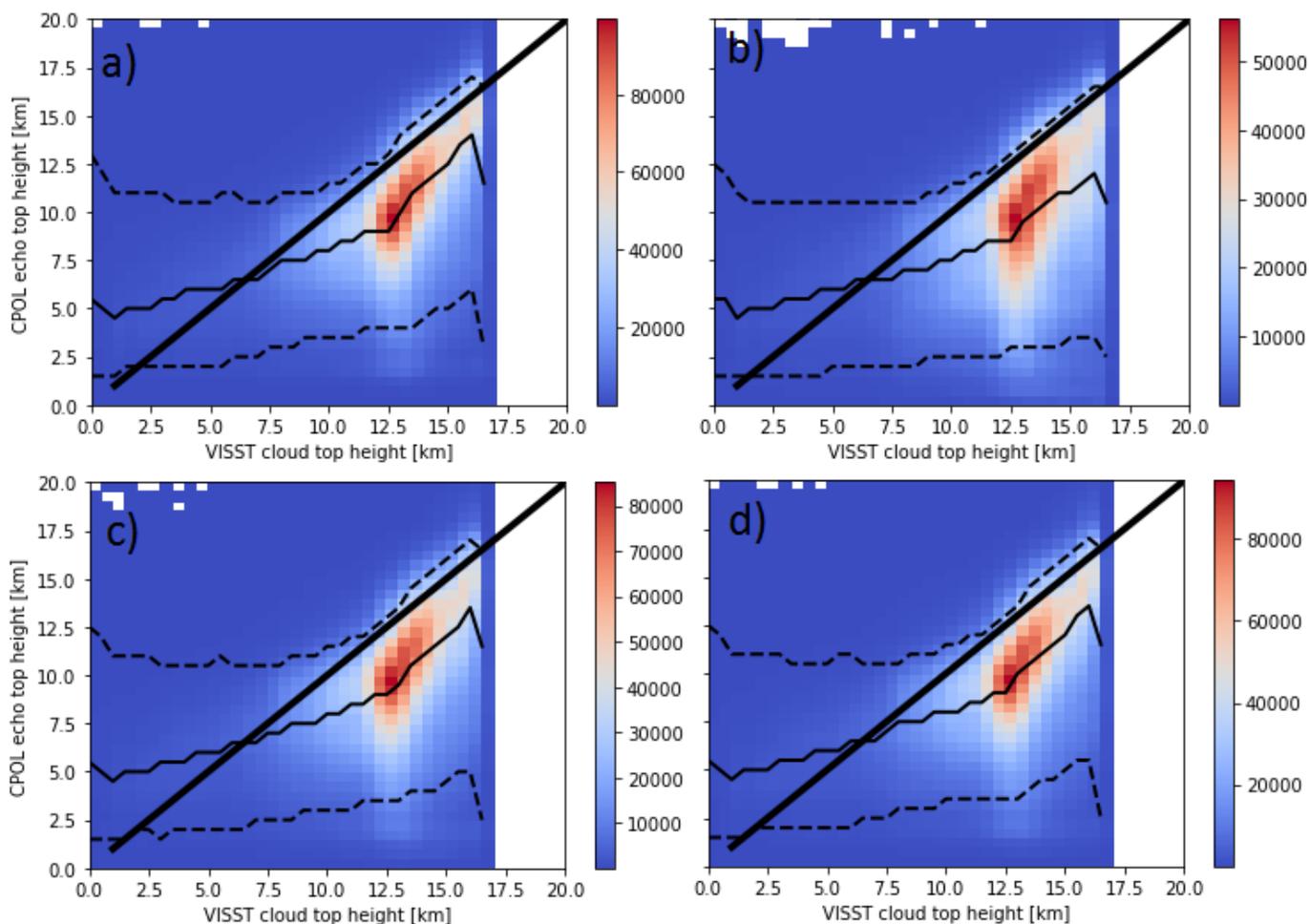
Figure 3. (a) ETH from CPOL retrieved using a Z threshold of 5 dBZ and (b) using a σ threshold of $2 \, m \, s^{-1}$. (c) using a σ threshold of $3 \, m \, s^{-1}$ and (d) $4 \, m \, s^{-1}$. The dashed lines represent the 5th and 95th percentiles of CPOL ETH, while the solid line represents the median of the CPOL ETH.
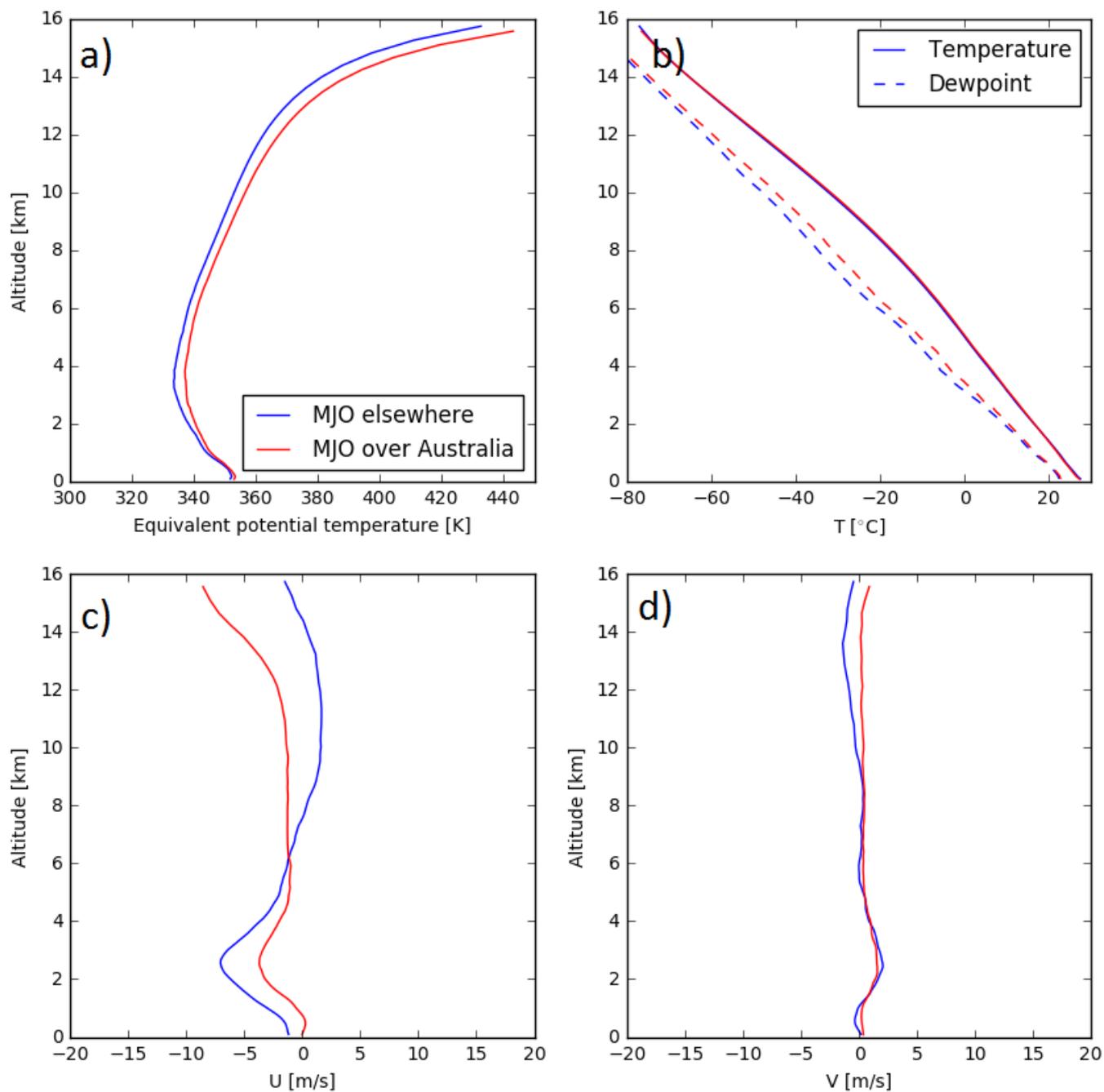
Figure 4. Mean vertical profiles of (a) equivalent potential temperature, (b) temperature and dew point, (c) zonal wind and (d) mean meridional wind from rawinsonde observations during break conditions.
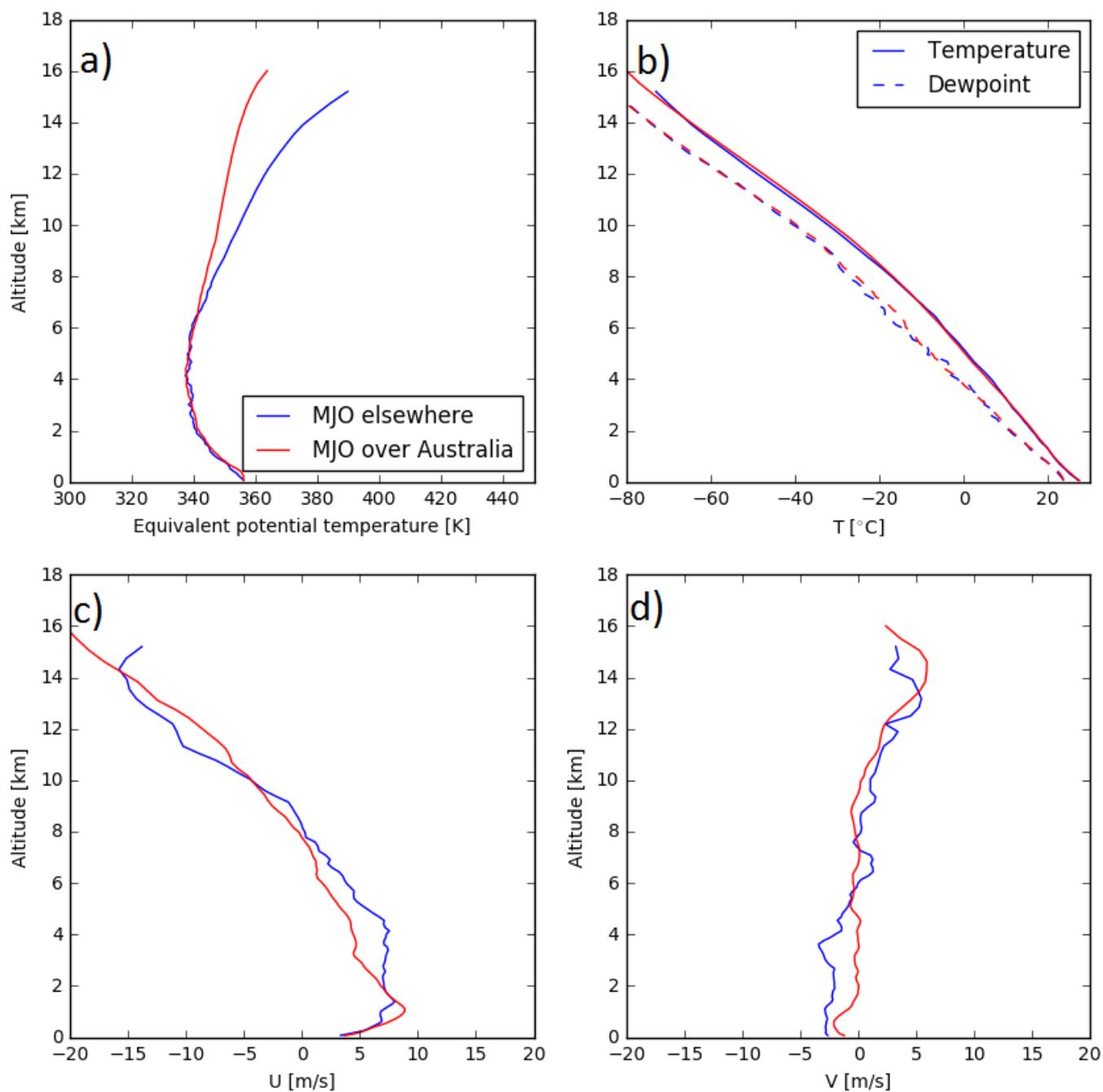
Figure 5. As Figure 4, but during active monsoon conditions.
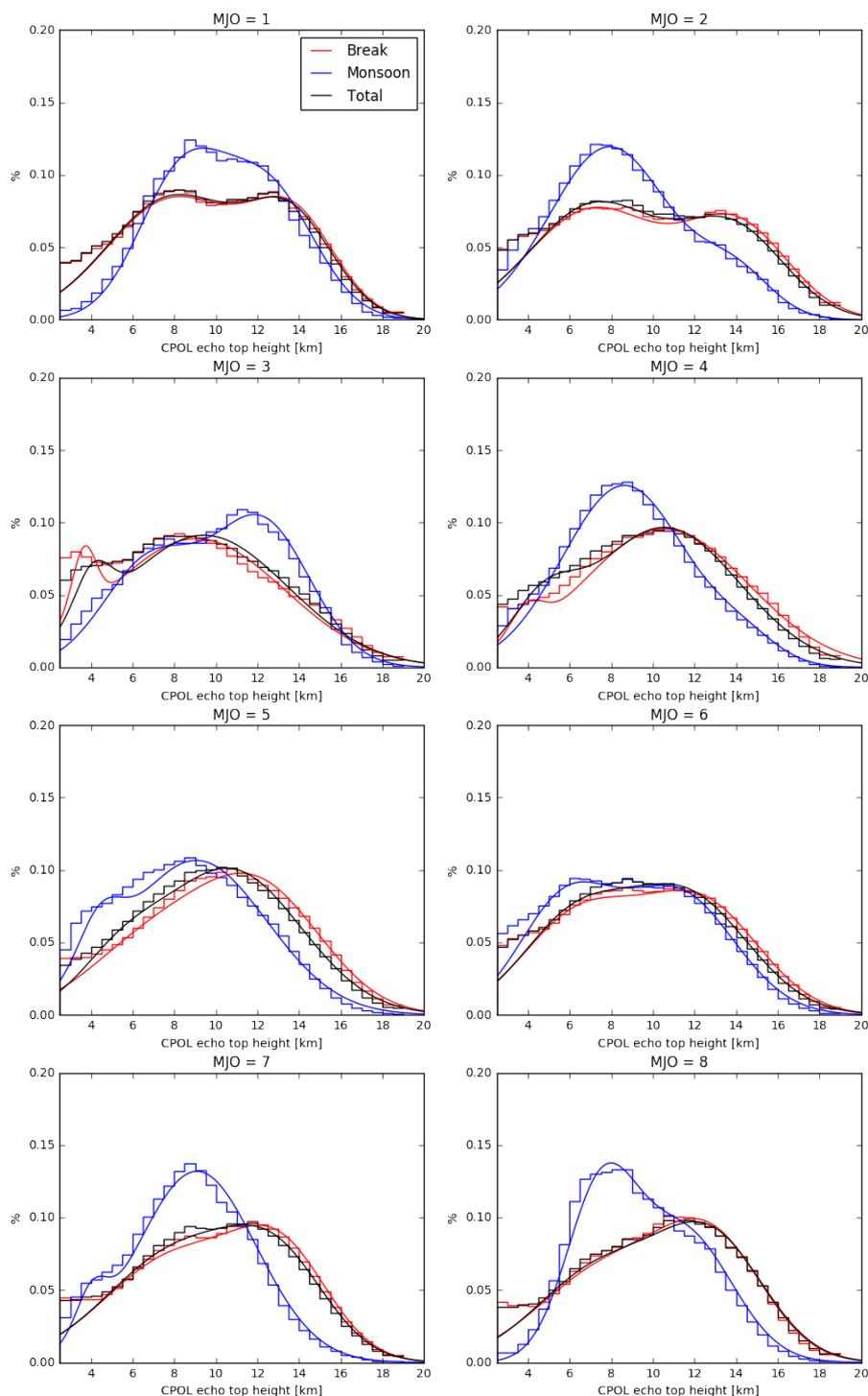
Figure 6. Normalized frequency distribution of ETHs in convective regions as a function of MJO index for break and monsoon conditions. Solid lines represent medians of modes derived from the fit of the bimodal Gaussian p.d.f. to the normalized frequency distribution.
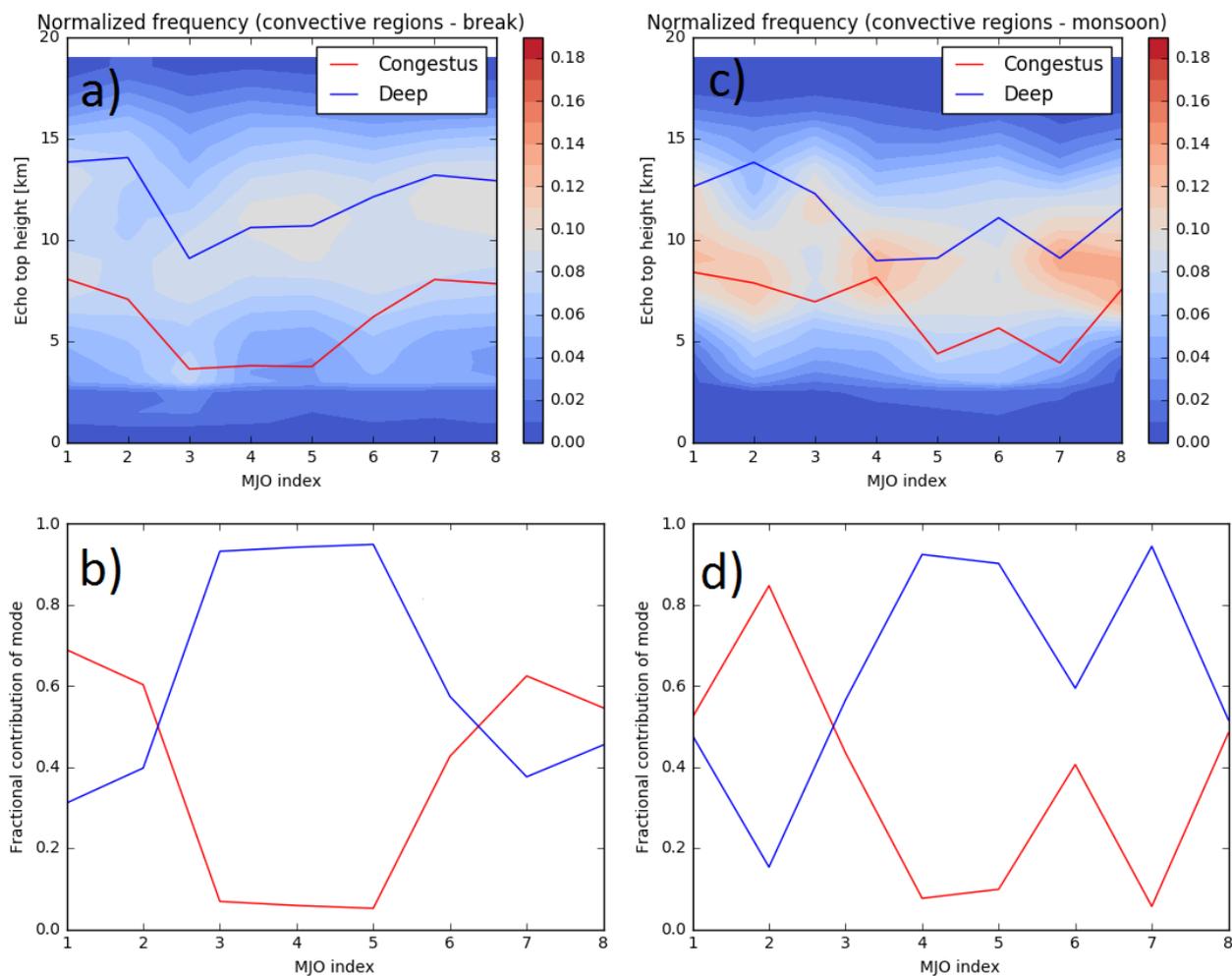
Figure 7. (a) p.d.f.s of ETHs in convective regions for given MJO indices in break conditions. The red line is μ_1 and the blue line is μ_2. (b) Fractional contribution of each mode (A (red line), 1-A (blue line)) to p.d.f.s in (a). (c,d) as (a,b) but for monsoon conditions.

Atmospheric
Chemistry
and Physics
Discussions
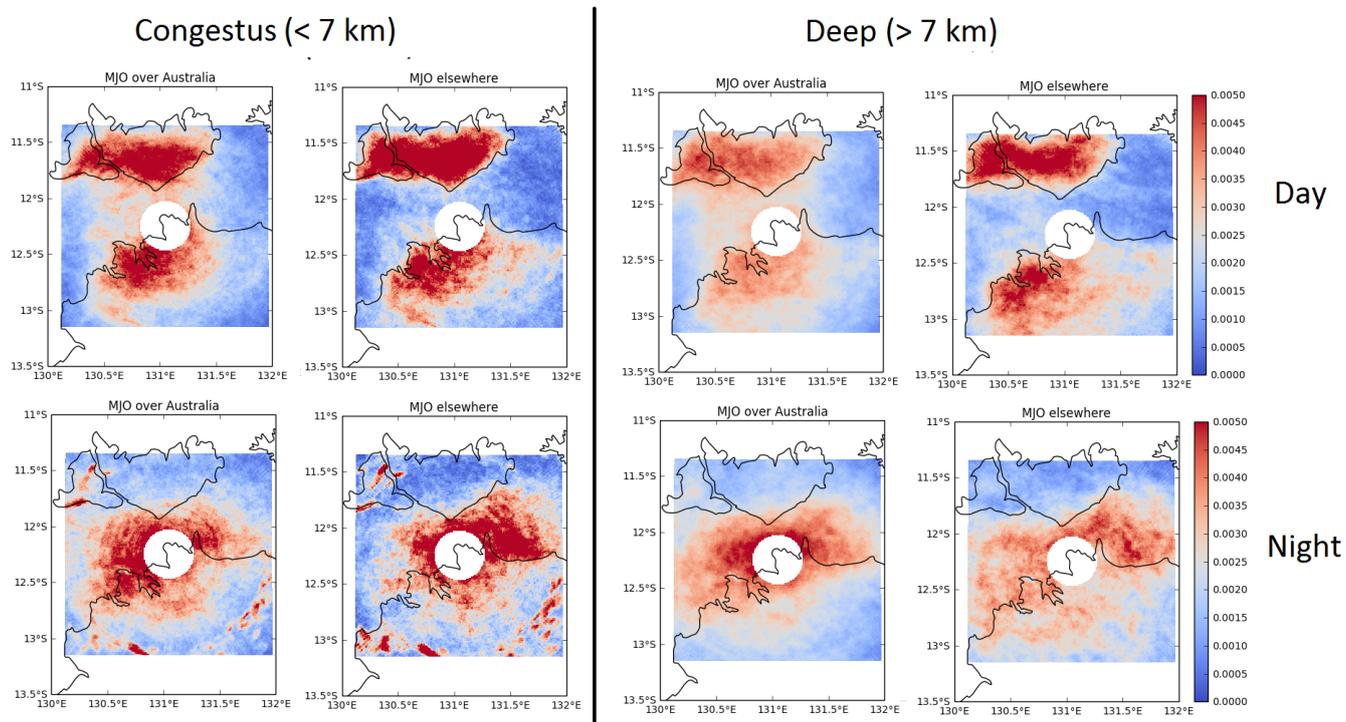
Figure 8. The normalized frequency of occurrence of ETHs < 7 km and > 7 km for given phase of the MJO during the day (21 to 10 UTC) and night (10 to 21 UTC).
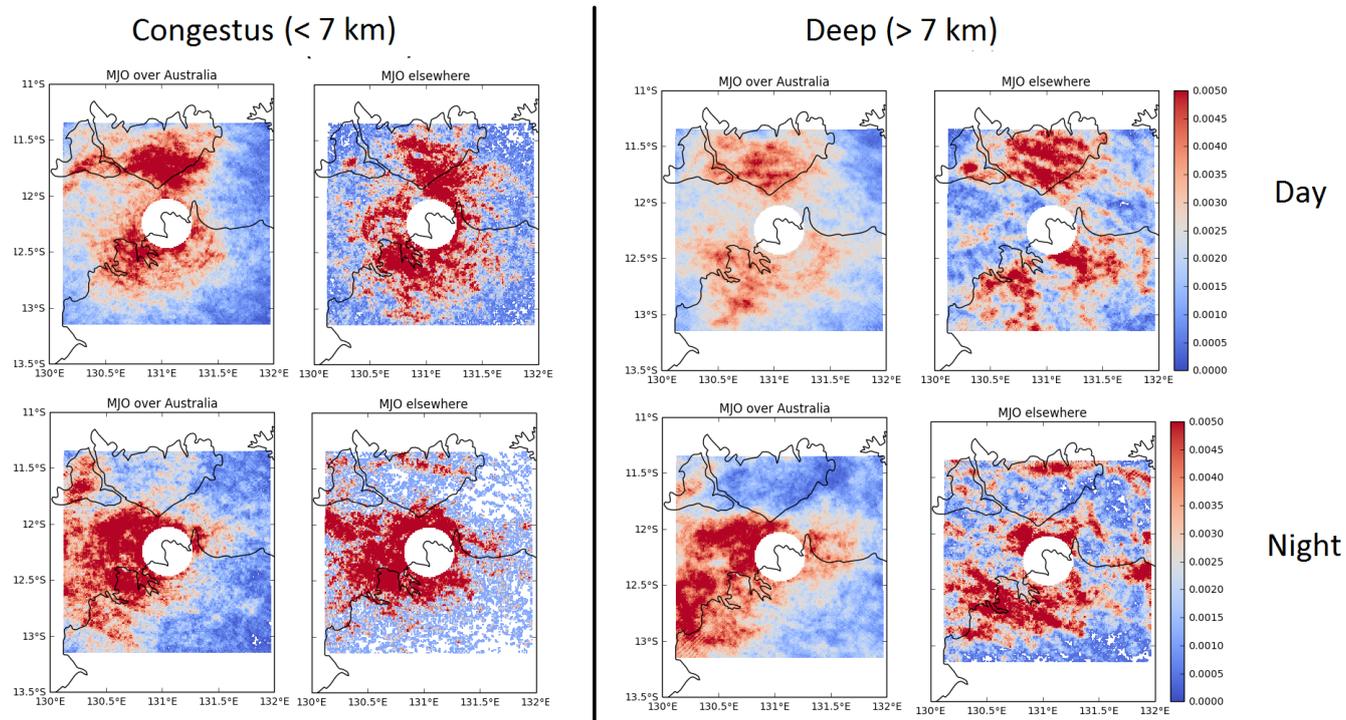
**Figure 9.** As Fig. 8, but for active monsoon conditions.
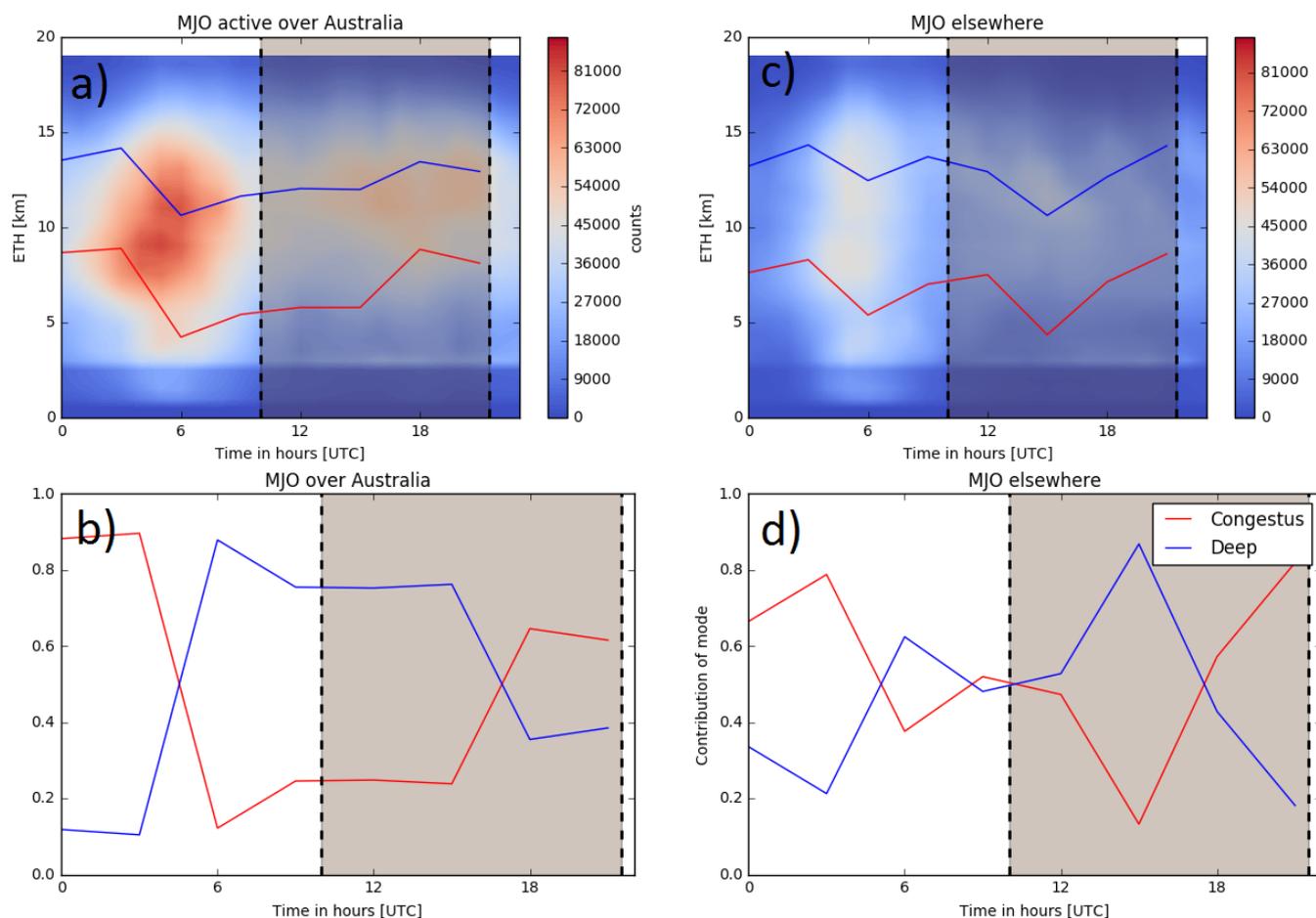
Figure 10. (a) Frequency distribution of occurrence of ETHs in convective regions as a function of time in break conditions when the MJO is active over Australia. Red line indicates peak of cumulus congestus mode, blue line indicates peak of deep mode of convection. (b) The contribution of the cumulus congestus mode A and deep mode 1-A to the p.d.f of ETH for the given hour. Shaded region indicates when it is night over Darwin. (c,d) as (a,b) but for when the active phase of the MJO is away from Darwin.

Atmospheric
Chemistry
and Physics
Discussions
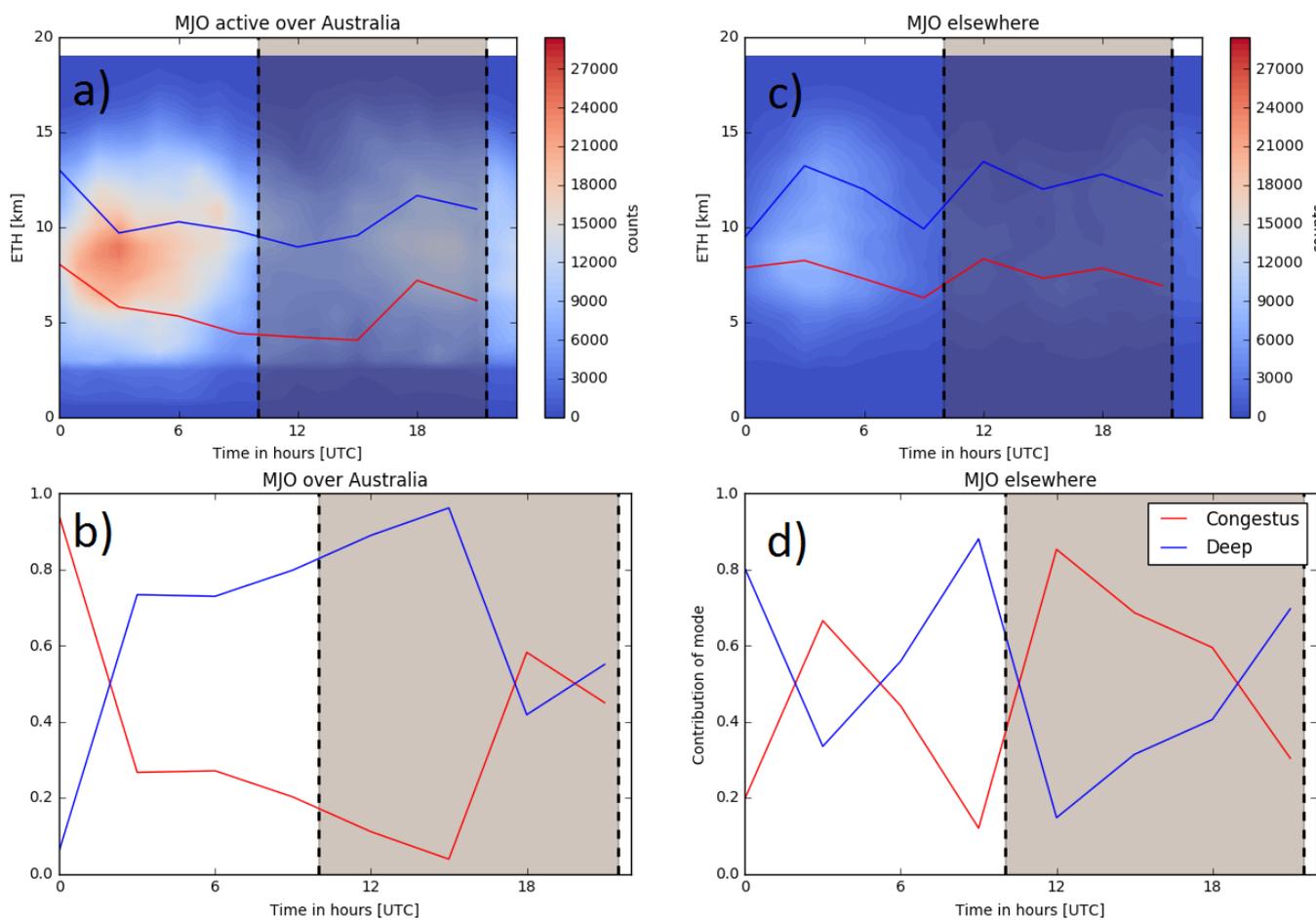
Figure 11. As Figure 10, but during active monsoon conditions.